Journal of Geochemical Exploration 218 (2020) 106615

Contents lists available at ScienceDirect

Journal of Geochemical Exploration

journal homepage: www.elsevier.com/locate/gexplo

Gossan mineralogy, textures, and gold enrichment over the Au (As, Bi, Ag) deposit in the Buracão Area (Brasília Fold Belt, Brazil): Implications for gold prospecting in weathering profiles

G.L.C. Pires[a,*], C. Renac[b], E.M. Bongiolo[c], R. Neumann[d]

[a] Instituto de Geociências, Universidade Federal do Rio de Janeiro – UFRJ, CEP 21941-916 Rio de Janeiro, RJ, Brazil
[b] Université Côte d'Azur, CNRS, Observatoire de la Côte d'Azur, IRD, Géoazur UMR 7329, FR 06560 Valbonne, France
[c] Instituto de Geociências, Universidade Federal do Rio Grande do Sul (UFRGS), Av. Bento Gonçalves 9500, Agronomia, CEP 90650-001 Porto Alegre, Brazil
[d] Centro de Tecnologia Mineral – CETEM, Divisão de Caracterização Tecnológica, CEP 21941-908 Rio de Janeiro, RJ, Brazil

ARTICLE INFO

Keywords:
Gold mineralization
Gossan mineralogy and textures
Gold chemical refining
Gold prospecting
Brasilia Fold Belt

ABSTRACT

The orogenic pyrite–rich Au (As, Bi, Ag) mineralization (up to 31 g/t) of the Buracão area is one of several orogenic deposits in the Brasilia Fold Belt (BFB; Central Brazil), exposed to tropical weathering that shows extensive oxidized profiles. The distribution and thickness of these gossan profiles lead to variable gold enrichments and uncertainties to gold prospecting in this region. In order to investigate physicochemical processes related to the evolution of the gossan cover and the supergene gold enrichment, we present mineralogical, textural and geochemical data from each zone of twenty gossan profiles in the Buracão area. These results show that the mineralogy and textures along the gossan profile reflect oxidation, hydrolysis, dissolution and precipitation processes controlled by different Eh–pH conditions, which are controlled by supergene conditions and hypogene ore composition. The geometry, distribution, and thickness of gossan profiles, as well as the style of gold occurrence, reflects textures of the hypogene orebodies, while the weathering has an important role in the gold chemical refining (i.e., increasing ca. 25% in gold fineness) and the distribution of gold grades along the profile.

These points allowed us to identify that the leached spongy hematite–rich zone in the upper indigenous profile contains the higher fineness gold grades (i.e., the "bonanza level"), and Bi–minerals such as waylandite and bismutite that may be important pathfinders for high gold grades in these gossan profiles. Our results demonstrate that ore prospection in gossans over Au–As–Bi–Ag deposits should be done focusing on leached zones, different to that traditionally conducted in gossans related to base metal sulfide deposits that have focused on precipitation zones. The similarities between the hypogene mineralization of the Buracão area and many deposits in the BFB and worldwide encourage the application of this approach elsewhere, which improve gold prospecting in weathering profiles over orogenic deposits.

1. Introduction

Gossan profiles produced by the interaction of surficial processes over sulfide–rich deposits have been the subject of many investigations in the last decade, due to their high-grade metallic composition and importance in environmental sciences (Reich and Vasconcelos, 2015; Dill, 2015; Vasconcelos et al., 2015). The evolution of a gossan profile is related to a series of inorganic and bio–induced supergene processes such as oxidation, hydration, and hydrolysis with millimeter to meter scale mechanisms of dissolution and precipitation recorded by mineralogical and textural changes (Thornber and Taylor, 1992; Nordstrom, 2003; Zammit et al., 2015). These physicochemical processes when developed over primary metalliferous ore deposits produce higher–grade supergene ores through physical and chemical refining mechanisms (Boyle, 1979; Leybourne et al., 2000; Robb, 2005). These ores are important both for their greater economic viability and for their importance as prospective guides for further discoveries of primary deposits at deeper levels (e.g., Scott, 1987; Gray et al., 1992). Thus, the identification of mineralogical and textural changes along the gossan profile is useful for chronological reconstructions of each physicochemical process and prospecting for the distribution of hypogene and higher–grade supergene orebodies (Velasco et al., 2013; Andreu et al., 2015; Yesares et al., 2015, 2017). In this way, much attention has been given to the supergene processes over base metal massive sulfide

* Corresponding author.
E-mail address: g.pires@geologia.ufrj.br (G.L.C. Pires).

https://doi.org/10.1016/j.gexplo.2020.106615
Received 16 March 2019; Received in revised form 4 May 2020; Accepted 18 July 2020
Available online 24 July 2020

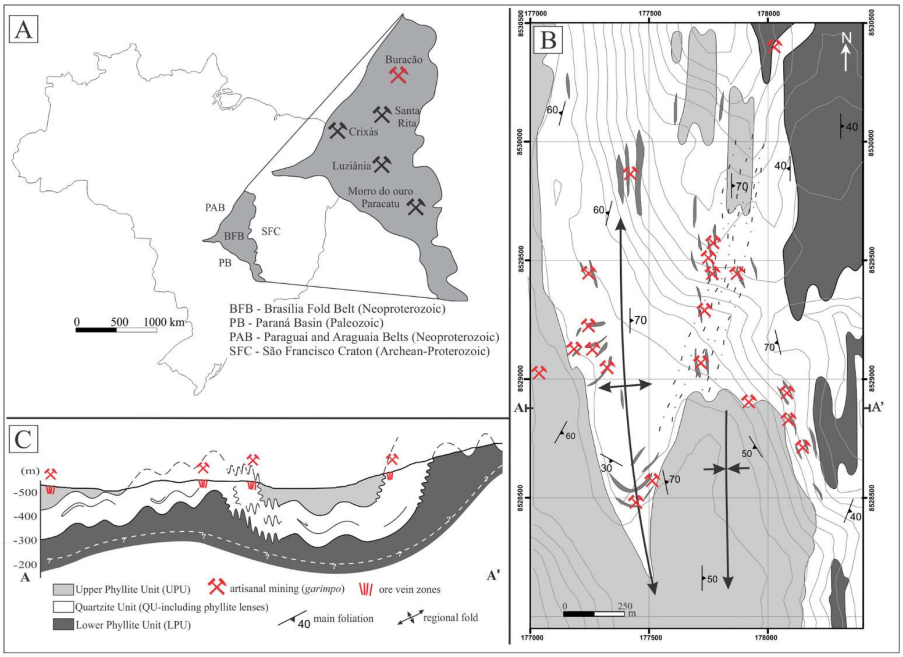

Fig. 1. Regional and local geological setting with: (A) location of the Buracão area and other well–known sulfide–rich orogenic gold deposits in the Neoproterozoic Brasília Fold Belt, Central Brazil; (B) simplified geological map of the Buracão area (1:10,000) with the location of the twenty artisanal minings (*garimpos*) studied in this work and (C) schematic W–E geological cross–section showing the disposition of ore vein zones and structural patterns of their host rocks in the Buracão area. (Simplified after Pires et al. (2016).)

deposits, whereas the supergene processes over Au–As–Bi–Ag orogenic deposits remains less studied, even considering this deposit type as the main gold source worldwide (e.g., Goldfarb et al., 2005).

In regions under tropical climate and tectonic stability as Central Brazil, weathering and erosion favor the development and preservation of extensive oxidized profiles. These features coupled with several occurrences of hypogene sulfide–rich orogenic gold deposits such as those of the Neoproterozoic Brasília Fold Belt (BFB; e.g., Dardenne and Botelho, 2014; Fig. 1A) make this region one of the most important to the study of gossan processes over this deposit type. In the Buracão area (northern section of BFB; Pires et al., 2016), twenty artisanal mining pits (*garimpos*; Fig. 1B) expose shallow gossan profiles developed over an orogenic Au (As, Bi, Ag) pyrite–rich mineralization (Pires et al., 2019). The distribution of gossan profile leads to variable gold enrichments and uncertainties to gold prospecting in this area.

The present work aims to investigate physicochemical processes related to the evolution of the gossan profile developed over the pyrite–rich Au (As, Bi, Ag) deposit in the Buracão area and their relation with supergene gold enrichment. The mineralogical, textural and geochemical data from each gossan zone presented here allow an interpretation of gold refining processes promoted by supergene processes and the spatial distribution of gold ore along gossan profiles. These results allowed us to elaborate a series of useful prospection guides for high gold grades based on mineralogy and textures. Moreover, the occurrence of a complete and exotic Bi-rich mineral speciation directly related to gold mineralization becomes the study area key for improving the prospection guide in Bi-rich gold deposits. This approach has important implications for gold prospecting in weathering profiles developed over many orogenic gold deposits.

2. Geological setting

2.1. Summary of the orogenic Au (As, Bi, Ag) mineralization in the Buracão Area

The orogenic Au (As, Bi, Ag) mineralization of the Buracão area (up to 31 g/t; Paringa Resources, 2012) occurs in subvertical structurally-controlled quartz veins (up to 3 m wide) exposed in twenty artisanal mining pits (cf. Pires et al., 2016; Fig. 1B). The ore–rich quartz veins are hosted in the quartzite-phyllite intercalation of the Traíras Formation, in the upper part of the Araí Group. This quartzite–phyllite intercalation represents a marine platformal sedimentation deposited in a Paleo–Mesoproterozoic rift-related basin (Tanizaki et al., 2015). These rocks were metamorphosed in greenschist facies and deformed in two ductile–brittle and brittle deformational phases during the Neoproterozoic Brasiliano Orogeny (Fig. 1C). The emplacement of ore veins with quartz and muscovite and traces of rutile, tourmaline, monazite, xenotime, epidote and sulfides are related to ductile–brittle deformation (Pires et al., 2016). The orogenic ore consists of dominant pyrite with traces of As and Bi with inclusions of less abundant arsenopyrite,

pyrrhotite, bismuthinite and chalcopyrite on intergrown with quartz and other gangue minerals. The analyses of sulfides and gold grains showed that gold occurs (i) as free nuggets of Au–Ag–Bi alloys classified as native gold (80% of nuggets) or electrum (20%), or (ii) as finely dispersed structural gold within pyrite (up to 0.5 wt%) and arsenopyrite (up to 1.2 wt%; Pires et al., 2019).

2.2. Holocene and present–day: climate and vegetation in Central Brazil

Local climate and vegetation features are presented here as a background for contextualizing the location and development of the studied gossan profiles. Paleoclimate reconstructions based on oxygen and carbon isotopes from calcareous stalagmites show that Central Brazil experienced alternant drier and wetter periods, with a cyclicity of ~208 years, during the last 33 thousand years (e.g., Novello, 2016). The present-day vegetation in the Buracão area, located within the Cerrado biome, is characterized by savanna–like vegetation, with scattered grasses and shrubs, twisted trunks, thick leaves, and long roots, which favor extensive exposure of rocks and soils (e.g., Furley, 1999). Present–day weather is related to a continental tropical climate with two well-defined seasons: dry and cold autumn-winter (daily temperature of ca. 24 °C; March to September) with wet (1600 to 1900 mm/year concentrated into strong tropical thunderstorms) and hot (average maximum daily temperature often 40 °C) spring-summer (September to March; e.g., Alvares et al., 2014).

3. Methods

3.1. Terminology, sampling and sample preparations

In this paper, we named *gossan* rocks formed by the interaction of surficial processes over sulfide ore, which includes oxidized, leached and enriched zones. This terminology includes not only the iron–bearing minerals but also other oxyhydroxides, clays, sulfates, phosphates, carbonates, selenides, secondary sulfides, and iodides among other minerals (e.g., Velasco et al., 2013). The different mineralogical and textural changes will define different *gossan maturity* or *gossan evolution* (cf. Scott et al., 2001). This work reports the term in situ to designate autochthonous or indigenous gossans developed over the primary vein zone, while the *precipitated gossanous crust* is used to designate the Fe– and Mn–rich material precipitated from circulating solutions (cf. Guilbert and Park, 1986).

We conducted detailed field descriptions to identify zonation of gossan profiles exposed in twenty artisanal mining pits, and sampling (whole rock and concentrates of minerals) in each zone to examine textural and mineralogical changes. Samples were screened by mineralogy and texture identified macroscopically. In each texture, mineralogy was detailed by the integration of petrography of thin and polished thick sections (reflected light and Scanning Electron Microscopy) coupled with Raman spectroscopy and X-ray diffraction (XRD) in powder preparations. Moreover, heavy-mineral concentration was obtained in each zone by panning, followed by electromagnetic, dense liquid and hand-picking separations (cf. Pires et al., 2019). Among heavy minerals, we collected gold grains to observe morphological changes and compare their chemical compositions with Au–Bi–Ag nuggets from the primary ore (Pires et al., 2019).

3.2. Optical and Scanning Electron Microscopy (SEM–EDS)

The mineralogical and textural identifications were obtained from reflected light microscopy and completed by Scanning Electron Microscopy (FEI Quanta 400 SEM) equipped with Energy Dispersive X-ray Spectroscopy detector (Bruker Quantax 800 system with an XFlash 6|60 silicon drift detector) at Centro de Tecnologia Mineral (CETEM) in Rio de Janeiro–Brazil. The semi–quantitative estimation of major elements proportions of mineral phases in atomic (at.%) and weight (wt%) was calibrated with lab standards of pyrite, hematite, Mn–oxides and Au–Ag–Cu–metals and silicates. Moreover, SEM–EDS allowed morphological observation of 226 gold nuggets as well as their Au, Ag and Bi atomic proportions. These qualitative analyses were used to calculate the fineness values (Fn = [100 × Au / (Au + Ag)]; Morrison et al., 1991).

3.3. Raman spectroscopy in thin and polished thick sections

Raman spectroscopy was conducted on thin and thick polished sections of gossanous material from all of the zones of the profiles in order to complete the mineral and textural characterizations. A Horiba Jobin–Yvon LabRam HR 800 Raman microprobe with He-Ne laser (632.8 nm at room temperature) excitation was used at CETEM/RJ. This technique was employed to distinguish iron oxides, secondary sulfides, sulfates and phosphates based on the CrystalSleuth database (Laetsch and Downs, 2006).

3.4. X–ray diffraction

After field and petrographic descriptions, the mineral characterization was conducted in whole gossan rock and mineral concentrates by X–ray diffraction (XRD). Spectra were collected on a Bruker-D4 Endeavor diffractometer with Co K_{α} radiation by a LynxEye detector over 4 to 80° 2θ at 250 s/step at CETEM. Analyses were conducted in backloaded powder preparations using DIFFRAC.EVA suite software (Bruker–AXS) and a PDF-4+ database (ICDD, 2018) for the identification of mineral assemblages.

3.5. Software–based thermodynamic modeling

Thermodynamic modeling was run using the PHREEQC software 3.4 (Parkhurst and Appelo, 2013) with LLNL database (Lawrence Livermore National Laboratory; Wolery and Sutton, 2013) in order to estimate the physicochemical conditions required to generate each mineral assemblage and texture observed in the gossan profile. In each model, it was calculated the conditions for the charge balance and redox equilibrium of an initial solution of pure water, as well as the saturation indexes of each modeled mineral for the equilibrium state. The initial solution (1 L) interacts with mineral assemblages observed in the hypogene and supergene minerals (10 mol of each mineral). Then, concentrations of the final solutions, pH and Eh in equilibrium, saturation indexes (i.e., saturated or undersaturated phases) and gain and loses initial phases were calculated.

4. Results

4.1. Structure and zonation of the gossan profile

Systematic field descriptions show that the gossan profiles have similar geometry, distribution and thickness in the twenty artisanal minings, reflecting the occurrence of hypogene sulfide–rich vein zones. The transition from sulfide–rich hypogene ore to the bottom of the gossan profile is gradual and represented by the first development of an assemblage of oxyhydroxides and sulfates (Fig. 2). A generalized gossan profile is composed of three distinct zones: the oxidation (lower) and leached (upper) zones developed above sulfide–rich quartz veins (i.e., indigenous gossan) and gossanized wall–rocks halos surrounding those (Fig. 3A). The indigenous gossan profile shows progressive changes of mineralogy and textures with an upward increasing proportion of iron oxides composing different mineral assemblages (Fig. 3B). The oxidation zone represents a partial pseudomorphic replacement of hypogene sulfides by an oxidized mineral assemblage in cellular boxwork structures (Fig. 3C), with minor precipitated material filling cavities and fractures (Fig. 3D and E). The leached zone shows an advanced replacement without relict hypogene sulfides. In this zone, the cellular boxwork structures observed in the lower oxidation zone appear with a more

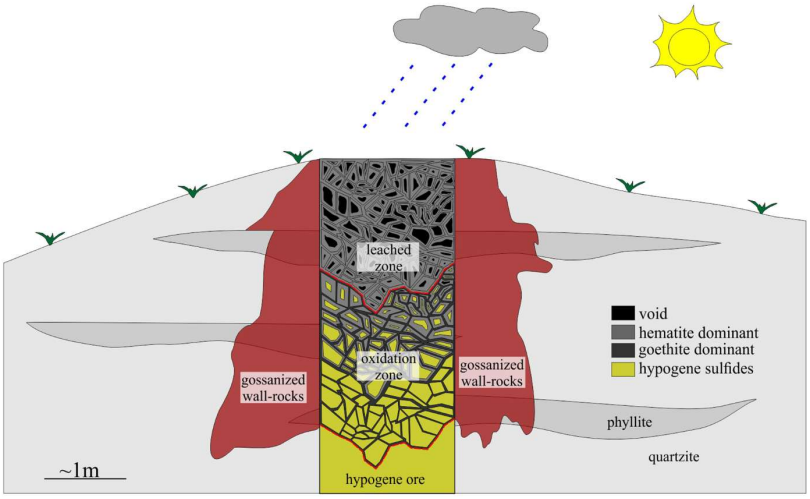

Fig. 2. Schematic cartoon showing the arrangement of gossan zones in the indigenous profile developed over the hypogene ore within vein zones and gossanized–wall rocks surrounding those.

porous or spongy aspect (Fig. 3F). The surrounding wall–rocks in the quartzite–phyllite unit show decimeter to meter–thick pervasively oxidation halos (Fig. 2) with gossanous crusts cementing crystal or lithic fragments (Fig. 3G). The pervasive precipitation in these halos increases at the vicinity of veins, obliterating textures of host rocks and developing oxyhydroxides crusts that achieve total rock replacement (Fig. 3H and I).

4.2. Mineralogy and textures of the oxidation zone

The oxidation zone is marked by the occurrence of gossan assemblage with residual hypogene sulfides in cellular boxwork structures (Fig. 4A to C). It is important to note that mineral and textural changes are so gradual that it is virtually impossible to observe all of them in the same polished section, so the descriptions below are based on several sections from the same or different locations. At the bottom of this zone, primary iron sulfide masses are replaced along existing fractures and grain boundaries by millimeter–thick goethite ribs (Fig. 4A and B). Goethite occurs with powdery habit in the immediate vicinity of relict sulfides and as colloform textures along the inner portions of the oxidation ribs (Fig. 4B). The colloform goethite contains traces of phosphorous, sulfur and silica compounds without visible crystals of phosphates, sulfates and silicates under SEM observation. Sulfates occur as prismatic crystals disseminated within goethite ribs (Fig. 4B and D), filling fractures or covering quartz masses (Fig. 4E and F). These sulfates comprise a dominant proportion of jarosite and melanterite, with less abundant barite, alunite, cannonite, amarillite and brochantite (e.g., Fig. 5 and Appendix 1). The mixtures of goethite and sulfates in oxidation ribs are accompanied by minor powdery covellite (Fig. 4B and D), as well as Se and I–rich minerals (Fig. 4G and H, respectively) that show atomic proportions corresponding to eucairite–selenojalpaite (Ag:Cu:Se) and iodargyrite (Ag:I; Appendix 2). Colloform goethite with traces of phosphorous is usually accompanied by euhedral to anhedral phosphates such as waylandite and vauxite founded along the zone (Fig. 5). Waylandite occurs always with subordinate bismite (with arsenic content up to 31 wt%; Appendix 2), and minor amounts of Bi–subcarbonates such as bismutite and beyerite (Fig. 5 and Appendix 1). They were identified as (i) anhedral masses filling fractures with Fe–, Cu– and Bi–sulfates and covellite (Fig. 4E), (ii) bismuthinite pseudomorphs within goethite (Fig. 4I) or (iii) as euhedral crystals covering gold nuggets (Fig. 4J). The goethite ribs become wider up to tens of centimeters while residual sulfide grains become smaller and scarcer in the upper levels. The decrease of sulfide proportion is accompanied by the increasing porosity in the cellular boxwork structures upwards in the zone (Figs. 2 and 4C).

The first occurrence of hematite was recognized ubiquitously in the middle level of the oxidation zone (Fig. 2). Hematite occurs as pseudomorphic to goethite ribs or as colloform textures infilling voids and fractures whatever the location (Fig. 4C). The proportion of hematite increases upwards whereas goethite decreases and becomes negligible in the top of the oxidation zone. Like goethite, hematite contains traces of As–, P–, S– and Si–bearing compounds without being observable on the SEM. The rest of primary sulfides, sulfates, covellite, selenides and iodides tend to vanish in the top of this zone. The oxidation zone also contains gold nuggets (up to 0.5 cm) surrounded by goethite, sulfates and hematite (Fig. 4B). These gold nuggets have usually similar flake to rounded morphologies compared with those from the hypogene ore (Fig. 6A and B), but with rough surfaces that contrast with smooth nuggets observed in the hypogene ore. This roughness is accompanied by the development of discontinuous Ag–Bi–depleted corrosion pits (up to 30 μm width; Fig. 6B), where Ag content become undetectable, differing to compositionally homogeneous Au–Ag–Bi nuggets from the hypogene ore (Fig. 6A).

4.3. Mineralogy and textures of the leached zone

The leached zone is marked by dominant pseudomorphic hematite and subordinate goethite without any sulfide. Based on several samples, it is notable that this zone shows spongy to rectangular boxwork structures with millimeter to centimeter-sized cavities and associated dissolution textures larger than those of the oxidation zone (Fig. 7A to C). Anhedral to euhedral waylandite, bismite, Au–Ag–Bi nuggets, vauxite, bismutite, beyerite and clays occur within pores (Fig. 5). They represent preserved minerals after dissolution and porosity

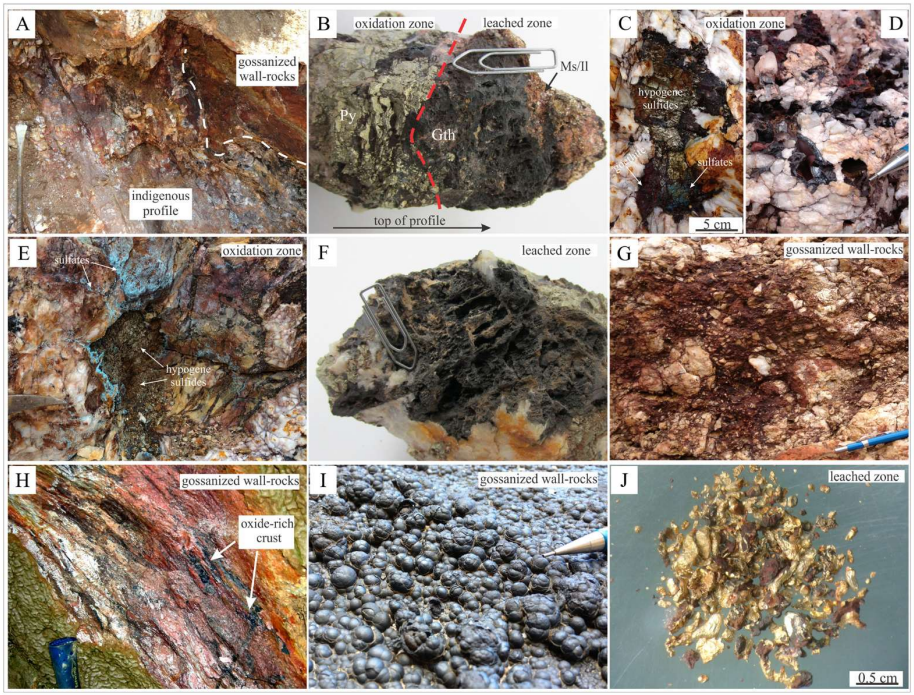

Fig. 3. Macroscopic aspects of each zone of the gossan profile. (A) General view of the disposition of indigenous gossan profile and surrounding gossanized wall–rocks (digging bar: 80 cm length); (B) hand sample showing the transition from sulfide–rich oxidation zone to oxide–rich leached zone in the indigenous profile (clip: 4 cm length). *Oxidation zone*: partial pseudomorphic replacement of hypogene sulfides by goethite and sulfates (C); precipitated colloform goethite filling voids (D; pencil: 2 cm length) and powdery sulfates along fracture surfaces (E; hammer: 15 cm length). *Leached zone*: hand sample showing hematite in rectangular to spongy boxwork structures (F; clip: 4 cm length). *Gossanized wall–rocks*: goethite–rich gossanous crust cementing crystal and lithic fragments in tectonic breccia cross–cutting quartz vein and quartzite (G; pencil: 8 cm length); (H) muscovite phyllite showing pervasive oxide–rich gossanous crusts developed along foliation plans (hammer: 10 cm length); (I) detail to Mn–oxyhydroxide gossanous crust showing botryoidal aspects replacing quartzite (pencil: 2 cm length). (J) Detail to panning concentrate of gold nuggets from the leached zone. Note strongly varied morphologies and sizes. (Py: pyrite, Gth: goethite, Ms: muscovite, Il: illite.) (For interpretation of the references to color in this figure legend, the reader is referred to the web version of this article.)

development. Hematite in the leached zone also contains traces of As–, P–, S– and Si–bearing compounds without crystalline shape (ca. 2 wt%), which increase in content upwards accompanying the increase of porosity (Fig. 7C). Thus, spongy boxwork structures at the upper levels of the leached zone are composed of As–, P–, S– and Si–richer hematite ribbing (Fig. 7D). At the upper level of the leached zone, pores and cavities are partially filled by botryoidal, acicular or microfibrous hematite textures (Fig. 7B and D). This hematite covers residual quartz and clays from veins to locally form a lateritic gossanous cap rock.

Like in the oxidation zone, leached zone shows coarse gold nuggets (up to 0.5 cm; Fig. 3J) surrounded by goethite and/or hematite observed on several samples (Fig. 7D and E). The morphology of gold nuggets varies more (e.g., flattened, elongated, rounded and flake shapes) than in the oxidation and hypogene ore. Nuggets have higher roughness with curved and twisted edges (Fig. 6C), compared with those from the oxidation zone and hypogene ore. Moreover, gold nuggets from the leached zone show wider Ag–Bi–depleted corrosion pits (> 100 μm width; Fig. 6C) than those from the oxidation zone, sometimes reaching almost the entire nugget. These corrosion pits show associated vermiform nanoporosity, which was observed with hematite filling or empty (Fig. 6C). In addition, fine gold particles (< 10 μm) with granular, flattened or flake–like shapes were found dispersed within spongy hematite in the upper levels of the leached zone surrounding coarse gold nuggets (Fig. 7E and F). The coarse gold nuggets consist of Au–Ag–Bi alloys, while the gold microparticles are pure Au. Comparing rims of coarse gold nuggets from the leached zone and hypogene ore, the fineness of the first is ca. 25% higher (ca. 900, equivalent to $Au_7AgBi_{0.1}$; measured in 134 grains) than those from the second (ca. 720, equivalent to $Au_2AgBi_{0.1}$; measured in 92 grains, Fig. 8). The increasing gold fineness in nuggets from the leached zone is related to decreasing proportions of Ag (from ca. 23.4 at.% in hypogene to 14.4 at.% in gossan ore) and Bi content (from ca. 0.5 at.% to 0.1 at.%; Fig. 8).

4.4. Mineralogy and textures of gossanized wall-rocks halos

This zone is marked by gossanous crusts developed through quartzite–phyllite host rocks surrounding the indigenous gossan profile

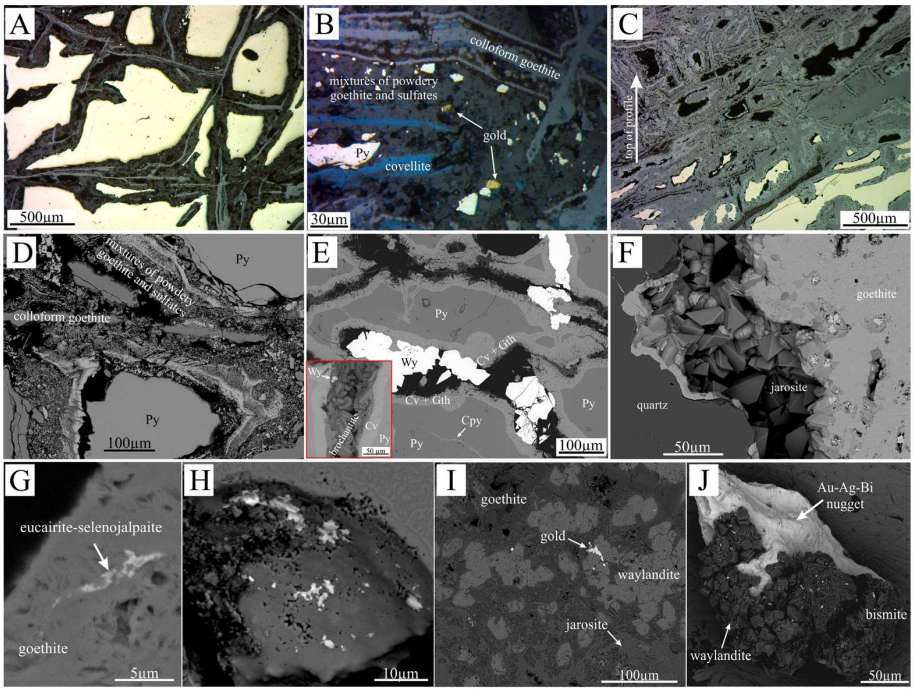

Fig. 4. Mineralogy and textures from the oxidation zone. (A), (B) and (C) reflected light photomicrographs of cellular boxwork structures from the bottom and the top of the oxidation zone, respectively. (A) Hypogene sulfide masses partially replaced by oxidation ribs in cellular boxwork structures with detail to (B) colloform goethite, gold nuggets as well as mixtures of powdery goethite, sulfates and covellite within the oxidation ribs. (C) Gradational decreasing of hypogene sulfides accompanied by increase of secondary porosity and the proportion of hematite over goethite. Backscattered electrons SEM image showing in detail (D) mixtures of powdery goethite, sulfates and covellite within oxidation ribs; (E) anhedral waylandite and prismatic brochantite filling fractures cross–cutting hypogene pyrite and chalcopyrite masses, which are partially replaced by goethite and covellite rims. Detail to (F) prismatic jarosite filling fractures; (G) anhedral eucairite–selenojalpaite and (H) iodargyrite within goethite pores; (I) waylandite as bismuthinite pseudomorphs within goethite and jarosite masses; (J) euhedral waylandite and bismite covering Au–Ag–Bi gold nugget. (Py: pyrite; Cpy: chalcopyrite; Cv: covellite; Gth: goethite; Wy: waylandite.) (For interpretation of the references to color in this figure legend, the reader is referred to the web version of this article.)

developed over ore–bearing veins. These crusts are composed of goethite, which is replaced by hematite at the upper portions of halos, and Mn–oxyhydroxides such as hollandite and lithiophorite. Hollandite (Mn-Ba oxide) shows ca. 6 wt% PbO and 1 wt% K_2O (Appendix 2), which suggest the presence of mixed minor phases as coronadite (Mn-Pb oxide) and cryptomelane (Mn-K oxide), all of them being end-members of the Coronadite Group (cf. Biagioni et al., 2013). Hollandite in contact with lithiophorite shows ca. 1 wt% of Al_2O_3, while lithiophorite ca. 3 wt% of BaO (Appendix 2) suggesting gradational transition between them.

Petrography reveals that these crusts occur infiltrated filling microfractures and surrounding quartz grains in quartzite or replacing phyllosilicates in phyllites. In the latter case, gossanous crust usually preserves phyllosilicates morphologies and the original foliated petrofabrics. In both lithologies, cubic pyrite pseudomorphs composed essentially of goethite might be observed. Petrography of several samples reveals that within gossanous crust goethite (or hematite) occur (i) in colloform textures combined with botryoidal shapes filling fractures (Fig. 9A), (ii) as fine acicular habits infilling negative sulfide boxworks (Fig. 9B), or (iii) coating crystal or lithic fragments in cockade to breccia–like textures (Fig. 9C and D, respectively). While Mn–oxyhydroxides occur always with goethite (or hematite) composing an intergrown cement with clay and quartz fragments in breccia–like textures (Fig. 9E) or as goethite surfaces covered by hollandite and then lithiophorite (Fig. 9F).

5. Discussion

5.1. Gossan evolution and processes related to the oxidation zone

The first occurrence of goethite with sulfates and covellite replacing hypogene sulfides in cellular boxwork structures represents the bottom of the oxidation zone. At this level, the dominant proportion of goethite covered by disseminated covellite and Fe, Cu and Bi–sulfates within boxwork porosity, oxidation ribs and fractures indicate sulfate precipitation later than goethite. These features suggest variable Eh–pH conditions, probably water table changes, controlling the saturation–undersaturation of these minerals. The precipitation of goethite suggests oxidative and slightly acidic Eh–pH conditions that favor the

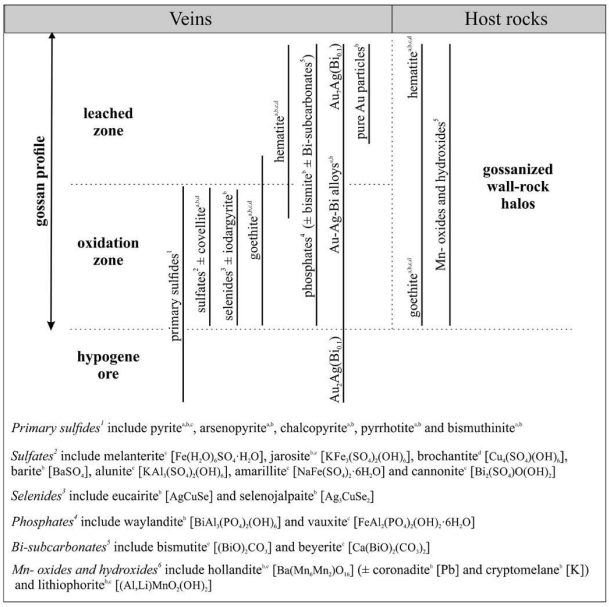

Fig. 5. Paragenetic mineral sequence through the indigenous gossan profile and gossanized wall–rock halos. Technique used for mineral characterization: [a]Optical microscopy, [b]Scanning Electron Microscopy equipped with Energy Dispersive System (SEM–EDS), [c]X-ray diffraction, [d]Raman spectroscopy.

replacement of primary Fe and Cu sulfides by goethite (Eq. (1): $FeS_{2(s)} + CuFeS_{2(s)} + 8\ O_{2(aq)} + 6\ H_2O_{(l)} \leftrightarrow 2\ Fe(OH)_{3(s)} + Cu^{2+}_{(aq)} + SO_4^{2-}_{(aq)} + 3HSO_{4(aq)} + 3H^{+}_{(aq)}$; Bigham and Nordstrom, 2000; Robb, 2005; Fig. 10A). This reaction indicates that Fe^{III} is trapped as goethite, with a mixture of hydrogen sulfide and sulfate ions in solution (Figs. 10A and 11A). These features are reinforced by the thermodynamic modeling that indicates conditions of pH 3.7 and Eh +0.2 V for the equilibrium of this reaction (Fig. 10A and Appendix 3). This model confirms that goethite is oversaturated while sulfates and sulfide minerals are undersaturated under these conditions. Moreover, the occurrence of jarosite, alunite, amarillite, barite and cannonite indicates Al, K, Na, Ba and Bi in solution, which reinforces the hydrolysis of aluminosilicates and Bi–minerals in the generation of these acidic fluids (e.g., Bigham and Nordstrom, 2000; Fig. 10A). The diachronous precipitation of goethite and sulfate minerals could be explained by the Holocene to present–day weather context. In this sense, episodes of intense rainfall as in wet seasons bring dissolved oxygen that would change hydrogen sulfide into sulfate ion, increasing its concentration, and still favors goethite stability. While in dry seasons, the lowering of the water table would restrict stationary fluids on grain and fracture surfaces. This lowering and associated evaporation would promote an increase of SO_4^{2-} ions concentration in residual water favoring the precipitation of Fe, Cu and Bi– sulfates (Fig. 11A). These features are consistent with the lack of a well–developed Cu–enrichment blanket, which indicates abrupt water table changes with rapidly alternant wet and dry seasons during the gossan evolution (e.g., Velasco et al., 2013; Fig. 11A). We assumed that the occurrence of Fe–rich sulfates and covellite replacing primary sulfides represent a cogenetic precipitation (Eq. (2): $CuFeS_{2(s)} + Cu^{2+}_{(aq)} + SO_{4(aq)}^{2-} \leftrightarrow 2CuS_{(s)} + FeSO_{4(s)}$; e.g., Evans, 1993), which indicates stationary Eh–pH conditions. The thermodynamic modeling indicates that covellite is oversaturated in association with goethite for equilibrium conditions of pH 3.7 and Eh + 0.2 V, while sulfate minerals remain undersaturated (Fig. 10A and Appendix 3). These conditions are similar to those from Eq. (1), suggesting that the covellite precipitation might be related to lowering of water table and saturation of hydrogen sulfide and sulfate ions in solution rather than contrasting changes of redox conditions. These features coupled with petrographic relationships indicate that the concentration of Cu–sulfate may have played an important role in the precipitation of covellite.

Eucairite, selenojalpaite and iodargyrite recognized in oxidation ribs reflect Se derived from Se–rich sulfides and Ag from Au–Bi–Ag alloys in the primary assemblage (Pires et al., 2019). Silver must have been leached out from gold nuggets through dealloying process (e.g., Erlebacher et al., 2001). These features are corroborated by rough surfaces and corrosion with the development of tens of micrometer Ag and Bi–depleted corrosion pits and nanoporosity in nuggets (Fig. 11B), contrasting with dominant smooth surfaces in those from the hypogene ore. The silver mobility under these redox conditions is also reinforced by thermodynamic modeling (Appendix 3). On the other hand, the lack of iodine in primary assemblages suggests its source associated with rainwater percolating through soils or external host rocks such as marine metasediments of the Araí Group (e.g., Tanizaki et al., 2015). Although petrographic and mineral observations are not enough to fully constrain the origin of iodine, we used thermodynamic databases to understand their precipitation processes. The LLNL database (Wolery and Sutton, 2013) indicates that selenides and iodides have lower Gibbs free energy than iron oxide, which favors their precipitation with respect to goethite. However, their saturation is rarely observed due to

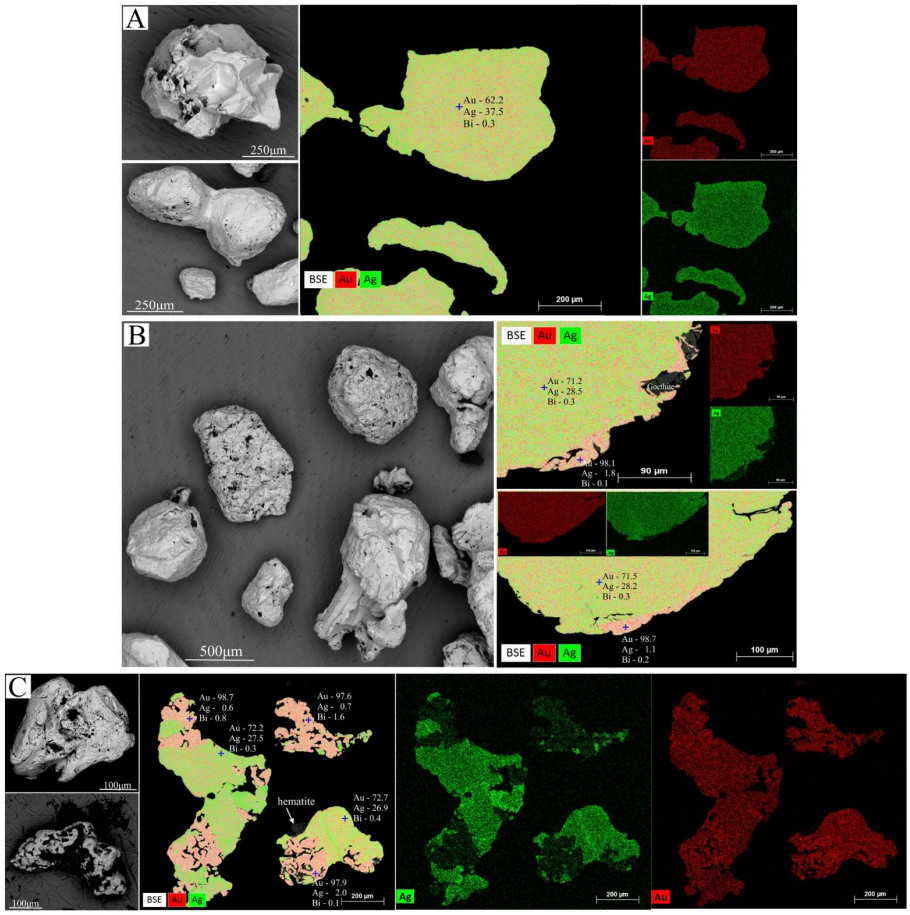

Fig. 6. Backscattered electrons SEM images and multi–element chemical maps showing morphologies, textures of surfaces, sizes and compositions of Au–Ag–Bi nuggets from (A) hypogene ore, (B) oxidation zone and (C) leached zone. Note the development of Ag–depleted corrosion pits accompanied by gold chemical refinement in nuggets from the gossan zones. Gold and silver contents from representative spot EDS analyses (blue crosses) are in at.%. (For interpretation of the references to color in this figure legend, the reader is referred to the web version of this article.)

low I and Se concentrations in percolating fluids. The occurrence of these minerals related to saline–halide rich groundwater formed by extreme evaporation rates (e.g., Andreu et al., 2015) leads us to interpret them as formed in dry seasons due high evaporation rates and lowering of the local water table (Fig. 11A).

Similarly, the occurrence of waylandite and bismite (i) associated with Fe, Cu and Bi–sulfates and covellite filling fractures, (ii) as bismuthinite pseudomorphs within goethite, and (iii) covering gold nuggets suggest fluids with Bi–, PO_4–, AsO_4–, Al–complexes in the oxidation zone. The presence of PO_4 anionic complex in fluids might be related to the hydrolysis of primary phosphate minerals (e.g., xenotime and monazite), while the occurrence of $H_2AsO_4^-$ (pH 2.5 to 7 and Eh > +0.5 V) substituting phosphoric or H_3AsO_3 and $AsS(OH)HS^-$ (Eh < +0.5 V; Wolery and Sutton, 2013) complexes are related to oxidation of arsenian pyrite or arsenopyrite in primary ore (Pires et al., 2019). Primary bismuthinite included within pyrite or Au–Ag–Bi nuggets are the suitable sources of Bi, which is consistent with decreasing Bi content in the Au–Ag–Bi alloys covered by hypogene Bi–phases. Therefore, the occurrence of Ag–Bi–depleted corrosion pits in gold nuggets coupled with the precipitation of silver– and bismuth–rich gossan minerals corroborate dealloying of Au–Bi–Ag nuggets as an important chemical gold refining mechanism, already effective in the oxidation

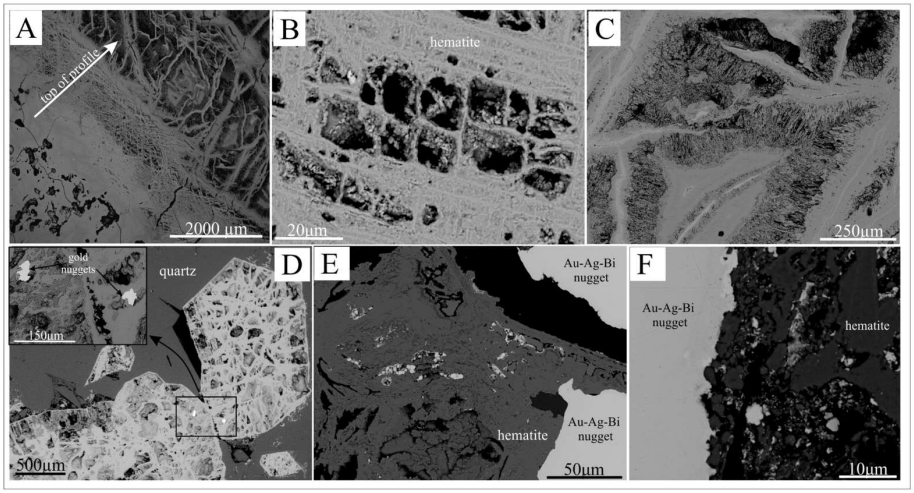

Fig. 7. Backscattered electrons SEM images showing mineralogy and textures from the leached zone. (A) General view of spongy boxwork structures developed by the increase of secondary porosity in hematite with detail to (B) rectangular boxwork structure partially filled by acicular to botryoidal hematite and (C) dissolution porosity developed preferentially in P, Si and S–poor hematite (darker gray) while richer ribbings (lighter gray) are preserved. (D) Sulfide pseudomorphs composed of P–, Si– and S–rich hematite ribbings with included gold nuggets (inset). Porosity is partially filled by botryoidal and microfibrous hematite. (E) Fine pure gold particles dispersed within porous hematite surrounding coarse Au–Ag–Bi nuggets with detail to (F) rough and corroded nugget boundaries.

zone (Fig. 11B). The wide occurrence of Bi–phosphates and oxides filling fractures and voids associated with Bi–sulfates is related to high–mobility of bismuth as ionic Bi^{III} under acidic and oxidizing conditions (Fig. 10B). However, these occurrences concentrated in the bottom of the oxidation zone indicate that their precipitation as Arsenic–bearing Bi–phosphates and oxides would be induced by an increase of Bi, PO_4–, AsO_4–complexes and O_2 dissolved in the fluid (Fig. 10B). The precipitation of these minerals would also be related to evaporation and fluid saturation in dry seasons. These features imply that the precipitation of these minerals is related to a later stage where Bi leached from bismuthinite and Au–Ag–Bi alloys precipitated as phosphate, sulfate and subcarbonate (Fig. 11A). Moreover, the dominant waylandite over sulfate and selenides coupled with its higher Gibbs free energy suggest that phosphates are more stable under oxidized-leaching conditions than sulfates and selenides, which favors their preservation (e.g., Gaboreau and Vieillard, 2004; Wolery and Sutton, 2013).

5.2. Gossan evolution and processes related to the transition to upper leached zone

Field and petrographic observations show that in the transition from the oxidation to the leached zone, gossan profile progressively shows cellular to spongy boxwork structures. These spongy structures are composed essentially of hematite with inclusions of anhedral to euhedral waylandite, bismite, Au–Ag–Bi nuggets, Bi–subcarbonates, and kaolinite. The change from cellular to spongy boxwork structures with the intensification of secondary porosity is accompanied by vanishes of sulfides and dissolution textures in iron oxides (Fig. 11C and D). These mineralogy and textures are consistent with infiltration of meteoric water, which dissolves sulfides and goethite, and stabilizes hematite. These features are reinforced by the thermodynamic modeling, which indicates that goethite is always undersaturated while hematite is oversaturated for equilibrium conditions of pH 7.4 and Eh + 0.5 V

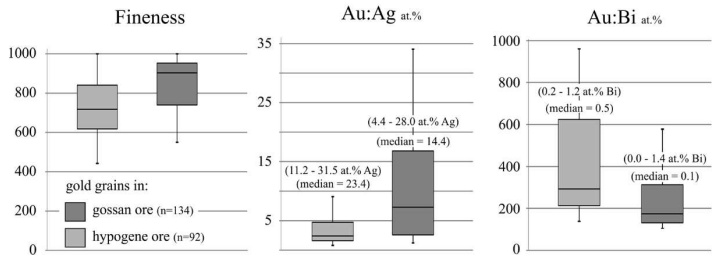

Fig. 8. Boxplot presentation of chemical composition of Au–Ag–Bi nuggets from the hypogene ore and leached zone.

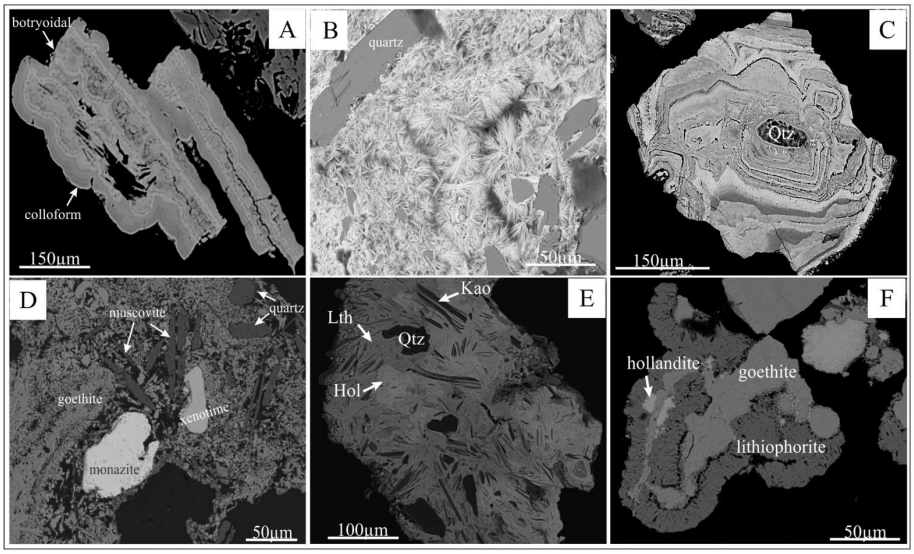

Fig. 9. Backscattered electrons SEM images showing mineralogy and textures from the gossanized wall–rock halos. Goethite in (A) colloform textures combined with botryoidal shapes filling fractures, (B) acicular habits infilling negative sulfide boxworks, and coating crystal or lithic fragments in cockade (C) to breccia–like textures (D). (E) Anhedral intergrown of hollandite and lithiophorite cementing quartz and kaolinite clasts and (F) goethite surfaces covered by hollandite itself covered by lithiophorite representing a local precipitation sequence (Qtz: quartz; Hol: hollandite; Lth: lithiophorite; Kao: kaolinite).

(Fig. 10B and Appendix 3). The modeling reinforces that goethite is dissolved and/or replaced by stable hematite while the rainfall water percolation front advances downstairs in the profile. The goethite dissolution also could be intensified by the presence of complex ligands such as organic chelates carried out by percolating meteoric water, which promote the formation of soluble Fe–chelate complexes (Zinder et al., 1986; Holmén and Casey, 1996).

We interpret the progressive predominance of hematite as a mark of the capillarity zone, which is formed by the lowering of the water table in dry seasons (Fig. 11C). The lowering of water table promotes dryness and access to oxygen, increasing oxidative conditions, evapotranspiration and dehydroxylation of goethite into hematite through dehydration processes (e.g., Tardy and Nahon, 1985; Goss, 1987; Martin, 2005; Fig. 11C and D). In addition, the lowering of the water table carries out ions in solution towards the bottom of the profile, concentrating them and favoring fluid saturation in the lower oxidation zone. Dissolution of residual sulfides and dehydroxylation of goethite may increase the porosity as observed at this level and promote supplementary fractures in boxwork textures (Fig. 11D). These physicochemical processes have been associated with the circulation of inorganic or organic complexes attested

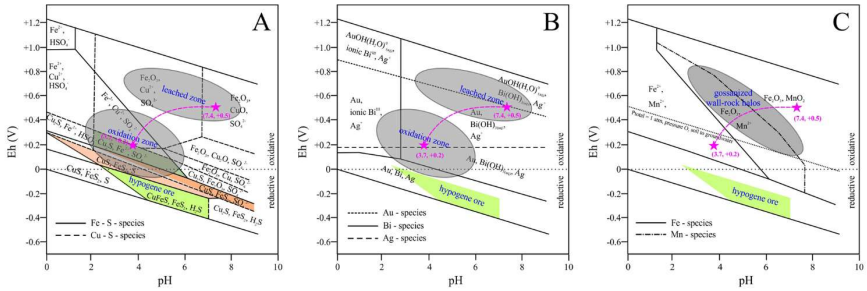

Fig. 10. Eh–pH stability diagrams for Fe, Cu, Bi, Ag, Au and Mn minerals and their related dissolved species including S and H_2O speciation at 25 °C and 1 bar (drawn using the CHNOSZ – R software package; Dick, 2008). Diagrams represent the chemical system of the indigenous gossan profile (A and B) and gossanized wall–rock halos (C; see text for explanation).

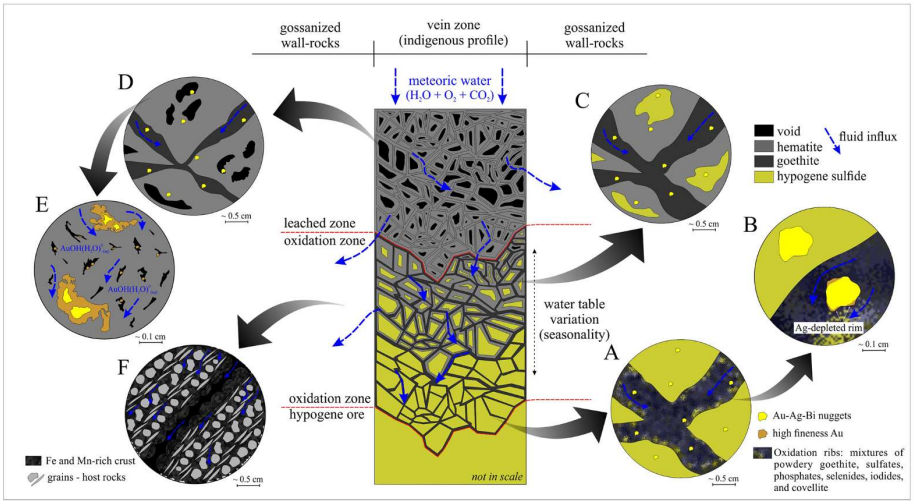

Fig. 11. Schematic geological model for the evolution of gossan profile and gold enrichment processes. (A) Hypogene sulfides are replaced by goethite along oxidation ribs of cellular boxwork structures. Precipitation of sulfates, phosphates, selenides, iodides and covellite are controlled by saturated stationary fluids under reducing conditions in dry seasons. (B) At this level, Ag is mobile and leached out from the Au–Ag–Bi nuggets through dealloying processes, which generate Ag–depleted corrosion pits in nuggets and increasing gold fineness, i.e., chemical gold refining acting since the oxidation zone. (C) The transition from the oxidation to leached zone marks the capillarity zone with higher oxidizing conditions coupled with longer air–dried exposition periods, which favor progressive predominance of hematite over goethite while relict sulfides progressively vanish. (D) The leached zone represents the stabilization of the capillarity zone with no sulfide preserved. At this level, higher volume of infiltrated water increases pH and Eh conditions, inducing dissolution of goethite and preservation of hematite with increasing porosity. (E) Strongly oxidizing conditions in the leached zone allow a weakly mobility of gold, which is leached out from coarse nuggets and precipitated as fine pure particles within porous hematite. These processes improve gold chemical refining that acts since lower zones. (F) Increasing Eh–pH of fluids derived from the lixiviation of the indigenous profile induce pervasive precipitation of Fe and Mn-rich crusts through the host rocks.

by the occurrence of As–, P–, S– and Si–rich compounds in hematite and goethite surfaces. These elements, derived from dissolution of arsenian sulfides, aluminosilicates and primary phosphates in veins and host rocks (Pires et al., 2019), have been adsorbed as inorganic or organic complexes (e.g., Arsenic, Dzombak and Morel, 1990). The accumulation of these surface complexes coupled with the weakly mobility of As, S, Si and P in supergene environment inhibit or reduce the dissolution of Fe–oxide and hydroxide (e.g., Biber et al., 1994).

Differing to the oxidation zone, the leached zone did not have iodargyrite, eucairite, selenojalpaite and sulfates. In this sense, the lack of these minerals may be associated with a high volume of percolating fluids in the upper part of the gossan profile, have solubilized, leached and carried down these ions towards the oxidation zone (Fig. 11). On the other hand, the waylandite and bismite in the leached zone confirm that these minerals are more stable under oxidized-leaching conditions than sulfates, selenides and iodide minerals. Moreover, the percolation of meteoric water favors the neutralization of acidity and allows the formation of Bi–subcarbonates found in the upper leached zone. These minerals must be related to HCO_3^- associated with rainwater or decomposition of organic matter.

The SEM petrography on coarse Au–Ag–Bi nuggets from the leached zone shows highly variable morphologies with nanometer–rough surfaces and curved and twisted edges associated with Au enrichment in corrosion pits. These nugget morphologies and chemical zonation contrast with chemically homogeneous nuggets from the hypogene ore, which evidence the influence of oxidation and rainfall weathering in gold alloys (e.g., Kalinin et al., 2009; Cruz et al., 2018). The change of $Au_2AgBi_{0.1}$ alloy in the hypogene ore to $Au_7AgBi_{0.1}$ in corrosion pits (an increase of ca. 25% in gold fineness) associated with Bi–rich phosphates and oxides in the hematite–rich zone confirms a gold chemical refinement related to rainfall and oxidative processes (Fig. 11E). The occurrence of pure Au microparticles within spongy hematite surrounding coarse Au–Ag–Bi nuggets indicate that these microparticles may be related to remobilization of some gold from coarse nuggets or “invisible” gold present within primary sulfide structures, rather than derived from the leaching of Ag and Bi (e.g., Wilson, 1984; Vasconcelos and Kyle, 1991; Kalinin et al., 2009; Fig. 11E). These features imply a weak mobility of gold in gossan profile as reported under tropical environments (e.g., Bowell, 1992; Bowell et al., 1993). The processes of gold refinement with gold mobility would imply oxidizing acidic to neutral conditions associated with thiosulfate, chloride, hydroxide and organic aqueous complexes (e.g., Boyle, 1979; Mann, 1984; Vlassopoulos and Wood, 1990). The lack of pure Au microparticles in the oxidation zone coupled with percolating rainfall water indicates that the concentration of ionic strength of thiosulfate, chloride and organic aqueous complexes must be insignificant to mobilize gold. On the other hand, the effective oxidizing conditions in the capillarity zone located in the upper level of the leached zone points out to S-bearing (e.g., HSO_3^-, $S_2O_3^{2-}$) complexes provided by organic matter or hydroxide aqueous complexes such as $AuOH(H_2O)^0_{(aq)}$ as the more reliable agents for gold mobility (e.g., Vlassopoulos and Wood, 1990; Fig. 10B). Although the thermodynamic modeling indicates that gold remains immobile (i.e., oversaturated) along the gossan profile (Appendix 3), the occurrence of Au microparticles in the capillarity zone suggests that only this zone shows physicochemical conditions favorable for gold mobility. These features become the leached zone a key for gold prospecting in the gossan profiles since it shows a dispersion halo.

5.3. Gossan evolution and processes related to the gossanized wall-rocks halos

The Fe– and Mn–rich gossanous crusts within quartzite–phyllite surrounding the entire indigenous gossan profile indicate the precipitation of cryptocrystalline or amorphous material such as am-Fe $(OH)_3$ and am-MnOOH directly from fluids (e.g., Larson, 1970; Martin, 2005; Fig. 11F). The occurrence of cryptocrystalline goethite, hollandite (± coronadite and cryptomelane) and lithiophorite in massive to microbanded textures represents the interaction of acid and Fe–rich oxidation fluid from indigenous gossan with the host rocks through a single or multiple fluid/host–rocks interactions (e.g., Pracejus et al., 1988; Martin, 2005; Fig. 11F). However, the occurrence of hollandite, coronadite and cryptomelane indicates Mn, Ba, Pb and K contributions of weathered minerals from the quartzite–phyllite package. The thermodynamic model with the saturation indexes of goethite, hematite, and pyrolusite for water under equilibrium with pH 7.4 and Eh + 0.5 V, indicates that goethite, hematite and MnO_2 are not simultaneously oversaturated. Observation of goethite and MnO_2 simultaneously combined with thermodynamic models indicates goethite (undersaturated) and Mn–phases (in equilibrium) represents a metastable stage of the gossaneous profile produced by a sequence of precipitation with goethite then MnO_2, where the first will be progressively replaced by hematite (i.e., oversaturated; Fig. 10C and Appendix 3). The mixed hollandite, coronadite and cryptomelane suggest that the precipitation of am-MnOOH was accompanied by absorption and/or adsorption of Ba, Pb and K (e.g., O'Reilly and Hochella, 2003; Vodyanitskii, 2009). On the other hand, lithiophorite could be formed by the interaction of precipitated Mn–oxyhydroxides with Al–clays such as kaolinite or with Al–complexes in fluids (e.g., Nahon et al., 1989; Varentsov, 1996). The occurrence of these crusts in host rocks surrounding both oxidation and leached zones of the indigenous profile suggest coeval continuous development with all stages of the indigenous profile. In addition, the occurrence of cryptomelane within Mn–rich gossanous crusts would allow radiometric dating, which could decipher the age of the main weathering episode and development of the gossan profile. Although, some gold occurrence has been reported in sulfide–rich hydrothermally altered host rocks (Pires et al., 2019), it was not observed within precipitated gossanous crusts. Therefore, the lack of gold in these gossanous crusts indicates that circulating fluids were not capable to mobilize gold from indigenous gossan profile towards the host rocks.

6. Conclusions

The mineralogical, textural and geochemical data presented here allow us to identify a series of physicochemical processes and reconstruct chronologically the evolution of the gossan profile over the Au (As, Bi, Ag) orogenic deposit in the Buracão area. Our results show that the mineralogy and textures along each gossan zone reflect physicochemical processes controlled by oxidative–reductive and pH conditions, which are resulted from the supergene environment and primary ore composition. Moreover, these results evidence that the geometry, distribution and thickness of gossan profiles, as well as the style of gold occurrence, strongly reflects textures of the hypogene orebodies. While the weathering has an important role in the gold chemical refining and the spatial distribution of gold grades along the gossan profile. Thus, based on these points, important environmental and exploration implications must be considered:

(a) Comparing the upper leached zone and the hypogene ore, the gold fineness increases up to ca. 25% upwards in the gossan profile;
(b) Spongy hematite–rich zone is the highest Au–grade ore zone of the profile, i.e., the "bonanza level" for gold prospecting in this environment, representing the more conspicuous textural and mineralogical indicators of the leached zone;
(c) Bi–minerals, especially waylandite and bismutite are important pathfinders for high gold grades in the gossan profile. This observation has a potential for improving the gold prospection through weathering profiles over Bi–bearing ore deposits;
(d) The occurrence of disseminated pure Au microparticles in the top of the gossan profile represents the development of a dispersion halo. These halos are important prospective guides in thick weathered profiles, such those in regolith mantles that have been successfully employed in the discovery of primary gold mineralizations in the Carajás Province, Amazon region, Brazil (e.g., Angelica et al., 1996; Costa et al., 1999);
(e) Although the gossanized wall-rock halo is the wider and more pronounced gossan zone, this zone is barren and irrelevant for gold prospecting.

The presented results demonstrate that ore prospecting in gossans developed over Au–As–Bi–Ag orogenic deposits should be different from that traditionally conducted in gossans over base metal massive sulfide deposits (e.g., Atapour and Aftabi, 2007; Kříbek et al., 2016). These differences reflect the mobility of base metals contrasting with weakly mobility to immobility of gold in the surficial environment. Differing to prospects for base metal deposits that should be directed to precipitation zones, prospects for gold in orogenic deposits should be done with a focus on leached zones. The similarities between the orogenic mineralization of the Buracão area and many deposits in the Brasilia Fold Belt and worldwide (see Pires et al., 2019) encourage the application of the presented approach for gold prospecting in weathered profiles. This approach improves substantially gold prospecting in gossans developed over many orogenic deposits.

CRediT authorship contribution statement

G.L.C. Pires: Conceptualization, Investigation, Writing - original draft. **C. Renac:** Conceptualization, Investigation, Writing - original draft. **E.M. Bongiolo:** Conceptualization, Investigation, Writing - original draft. **R. Neumann:** Conceptualization, Resources, Writing - original draft.

Declaration of competing interest

I state that there is no conflict of interest.

Acknowledgments

The authors thank the Paringa Mineração Ltda, in particular to Paulo Ilídio de Brito and Mauricio Prado for support during fieldwork and the CETEM staff, the technicians Josimar Lima and Edivaldo Silva, for their help during analytical procedures; anonymous reviewers and the Editor-in-Chief Stefano Albanese of Journal of Geochemical Exploration for suggestions that improved earlier versions of the manuscript. G.L.C. Pires also thanks to the Coordination of Superior Level Staff Improvement – CAPES/Brazil for post-doctoral PNPD scholarship (grant # 1733827). E.M. Bongiolo and R. Neumann thank the National Council for Scientific and Technological Development – CNPq/Brazil for his Research on Productivity (grant # 300936/2016-8) and his financial support (grant # 302828/2015-0), respectively.

Appendix 1. Representative powder X–ray diffraction patterns of whole–gossan samples from oxidation, leached and gossanized wall–rock zones

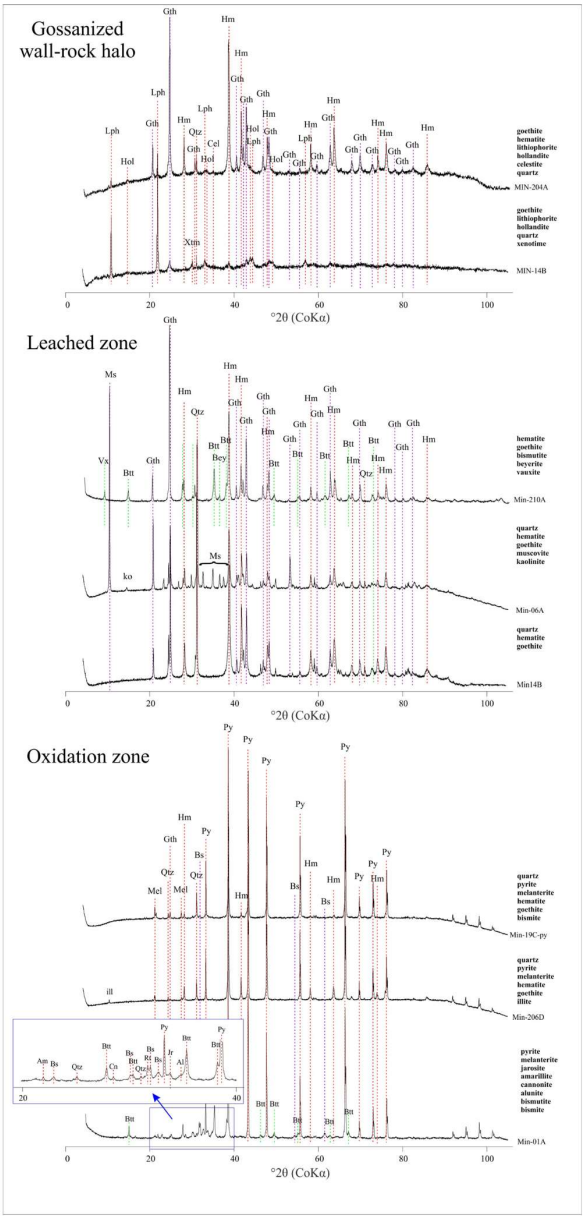
Gossanized wall-rock halo
Leached zone
Oxidation zone
goethite
hematite
lithiophorite
hollandite
celestite
quartz
MIN-204A
goethite
lithiophorite
hollandite
quartz
xenotime
MIN-14B
hematite
goethite
bismutite
beyerite
vanxite
Min-210A
quartz
hematite
goethite
muscovite
kaolinite
Min-06A
quartz
hematite
goethite
Min14B
quartz
pyrite
melanterite
hematite
goethite
bismite
Min-19C-py
quartz
pyrite
melanterite
hematite
goethite
illite
Min-206D
gyrite
melanterite
jarosite
amarillite
cannonite
alunite
bismutite
bismite
Min-01A
°2θ (CoKα)

Appendix 2. Chemical composition of main Bi–, Cu– and Mn–phases. Mineral structural formulae were calculated on data expressed in at. % based on EDS analyses

Oxidation zone

(wt%)	Fe_2O_3	Bi_2O_3	Al_2O_3	P_2O_5	As_2O_5	Total
Waylandite $[Bi_{(0.8–2.2)}Al_{(1.8–3.3)}(\{P_{(0.5–0.8)},As_{(0.2–0.5)}\}O_4)_2(OH)_6]$						
01		56.4	27.5	16.3		100.2
02		58.8	26.3	14.8		99.9
03	3.1	60.5	22.0	14.0		99.6
04	4.6	59.4	20.7	15.2		99.9
05	1.1	51.4	29.0	18.5		100.0
06		46.6	30.9	22.5		100.0
07		74.5	14.7	10.8		100.0
08	0.8	48.1	29.9	20.7	0.4	99.9
09	1.5	50.6	27.6	19.6	0.5	99.8
10	3.0	44.2	31.0	21.9		100.1
11	2.6	49.4	27.8	20.2		100.0
12		42.1	15.8	10.8	31.3	100.0
13	10.2	42.7	16.9	10.2	20.0	100.0
Bismite $[Bi_{(1.4–1.8)}Fe_{(0–0.8)}As_{(0–0.6)}O_3]$						
01	7.7	92.3				100.0
02	3.7	96.3				100.0
03	12.0	87.0				99.0
04	1.9	98.1				100.0
05	14.6	85.4				100.0
06	7.3	92.7				100.0
07	8.5	91.5				100.0
08	2.6	97.4				100.0
09	40.5	49.9	10.5			100.9
10	2.7	80.4	15.7			98.8

Oxidation zone

(wt%)	Fe	Cu	S	Ag	Se	Total
Eucairite-selenojalpaite $[Ag_{(1.1–3.2)}Cu_{(1.0)}Fe_{(0–0.3)}Se_{(1.6–2.6)}]$						
01		16.3		45.3	38.4	100.0
02		10.4		56.3	33.3	100.0
03	16.8	17.2		31.4	34.6	100.0
04		20.4		38.4	41.2	100.0
Covellite $[Fe_{(0.1–0.2)}Cu_{(1.0)}S_{(0.9–1.1)}]$						
01	4.5	62.6	32.2	0.6		100.0
02	4.8	61.0	34.0	0.3		100.0
03	5.9	62.0	29.4			97.3
04	7.2	60.8	30.8	0.6		99.3
05	1.4	66.6	30.6			98.6
06	3.5	67.1	29.0			99.6
07	0.9	66.6	31.4			99.0
08	3.5	64.7	30.7			98.9

Oxidation zone

(wt%)	Ag	I	Total
Iodargyrite $[Ag_{(1.0)}I_{(0.8)}]$			
01	47.7	52.3	100.0
02	44.6	55.4	100.0
03	48.6	51.4	100.0
04	45.2	54.8	100.0

Gossanized wall-rocks halos

(wt%)	Fe_2O_3	SiO_2	Al_2O_3	MnO_2	BaO	PbO	K_2O	Total
Hollandite (± Coronadite, Cryptomelane)								
01	3.3		1.3	73.5	14.1	2.0		94.2
02			6.7	71.6	6.8	9.7		94.9
03	2.8			77.1	14.9			94.8
04	2.1			74.4	18.3			94.8
05			0.6	84.4	8.7		1.2	94.9
06	2.6	2.7		77.3	10.5	1.8		94.8
07	1.0			76.1	17.7			94.8
08			0.7	81.6	11.7		0.9	94.8
09		2.3	3.6	77.8	10.1		1.2	95.1

10		0.6	1.0	78.4	8.5	1.1	89.6
11		0.7	0.6	81.1	12.1	0.3	94.8
12	2.8			77.4	15.0		95.2
13	2.1			74.7	18.3		95.2
14				77.9	17.3		95.2
15	1.0			76.4	17.8		95.2
16				83.9	11.3		95.2
17	0.8			78.5	16.0		95.2
18	2.2			82.1	10.8		95.2
19		0.9		87.6	6.3		94.7
20				77.6	17.2		94.8
21				83.6	11.2		94.8
22	0.8			78.1	15.9		94.8
23	2.2			81.8	10.8		94.8
Lithiophorite							
01	1.3		19.3	60.2	2.8		83.5
02		1.2	28.8	53.5			83.5
03	1.1		23.8	57.2			82.2
04			25.2	55.4			80.6

Appendix 3. Summary of thermodynamic modeling and estimated redox conditions. Undersaturated minerals in red and oversaturated in black

Leached zone and gossanized wall-rock halos

Solution composition: pH = 7.4, Eh = +0.5 V, activity of water = 1.00, T = 25 °C, P = 1 atm

Element	mol L^{-1}	Phase	SI	log IAP	log K(T,P)	Initial	Final	Delta
Ag	9.50E−07	Ag°	−0.00	7.99	7.99	1.00E+01	1.00E+01	−9.50E−07
Au	7.89E−22	Au°	−0.00	−7.09	−7.09	1.00E+01	1.00E+01	8.27E−18
Fe	1.26E−12	Goethite	−0.49	0.04	0.53	1.00E+01	0	−1.00E+01
Mn	4.75E−07	Hematite	−0.00	0.08	0.08	1.00E+01	1.50E+01	5.00E+00
		Pyrolusite	−0.00	−17.66	−17.66	1.00E+01	1.00E+01	−4.75E−07

Oxidation zone

Eq. (1): $FeS_{2(s)} + CuFeS_{2(s)} + 8O_{2(aq)} + 6H_2O_{(l)} \leftrightarrow 2Fe(OH)_{3(s)} + Cu^{2+}_{(aq)} + SO^{2-}_{4(aq)} + 3HSO^{-}_{4(aq)} + 3H^{+}_{(aq)}$

Solution composition: pH = 3.7, Eh = +0.2 V, activity of water = 0.52, T = 25 °C, P = 1 atm

Element	mol L^{-1}	Phase	SI	log IAP	log K(T,P)	Initial	Final	Delta
Ag	1.07E−10	Ag°	−0.00	7.99	7.99	1.00E+01	1.00E+01	−1.07E−10
Au	6.55E−26	Au°	0.00	−7.09	−7.09	1.00E+01	1.00E+01	1.79E−15
Cu	6.08E+00	Brochantite	−0.00	15.42	15.42	1.00E+01	4.36E+00	−5.64E+00
Fe	2.81E+01	Chalcocyanite	−4.74	−1.83	2.91	1.00E+01	0	−1.00E+01
K	1.00E+01	Jarosite	−1.15	−10.56	−9.41	1.00E+01	0	−1.00E+01
S	3.92E+01	Goethite	−0.00	0.53	0.53	1.00E+01	3.19E+01	2.19E+01
		Covellite	−0.00	−22.86	−22.86	1.00E+01	4.65E+01	3.65E+01
		Chalcopyrite	−12.30	−44.91	−32.60	1.00E+01	0	−1.00E+01
		Pyrite	−20.98	−45.68	−24.70	1.00E+01	0	−1.00E+01

Oxidation zone

Eq. (2): $CuFeS_{2(s)} + Cu^{2+}_{(aq)} + SO^{2-}_{4(aq)} \leftrightarrow 2CuS_{(s)} + FeSO_{4(s)}$

Solution composition: pH = 3.7, Eh = +0.2 V, activity of water = 0.52, T = 25 °C, P = 1 atm

Element	mol L^{-1}	Phase	SI	log IAP	log K(T,P)	Initial	Final	Delta
Ag	1.07E−10	Ag°	−0.00	7.99	7.99	1.00E+01	1.00E+01	−7.38E−12
Au	6.55E−26	Au°	−0.00	−7.09	−7.09	1.00E+01	1.00E+01	1.00E−10
Al	9.17E−04	Alunite	0.00	−0.47	−0.47	1.00E+01	1.00E+01	−3.06E−04
Cu	6.08E+00	Brochantite	0.00	15.42	15.42	1.00E+01	4.36E+00	−5.64E+00
Fe	2.81E+01	Chalcocyanite	−4.74	−1.83	2.91	1.00E+01	0	−1.00E+01
K	1.00E+01	Jarosite	−1.15	−10.56	−9.41	1.00E+01	0	−1.00E+01
S	3.92E+01	Melanterite	−0.60	−3.00	−2.40	1.00E+01	1.00E+01	0
		Goethite	0.00	0.53	0.53	1.00E+01	3.19E+01	2.19E+01
		Covellite	−0.00	−22.86	−22.86	1.00E+01	4.65E+01	3.65E+01
		Chalcopyrite	−12.30	−44.91	−32.60	1.00E+01	0	−1.00E+01
		Pyrite	−20.98	−45.68	−24.70	1.00E+01	0	−1.00E+01

References

Alvares, C.A., Stape, J.L., Sentelhas, P.C., Gonçalves, J.L.M., Sparovek, G., 2014. Köppen's climate classification map for Brazil. Meteorol. Z. 22 (6), 711–728.

Andreu, E., Torró, L., Proenza, J.A., Domenech, C., García-Casco, A., Villanova de Benavent, C., Chávez, C., Espaillat, J., Lewis, J.F., 2015. Weathering profile of the Cerro de Maimón VMS deposit (Dominican Republic): textures, mineralogy, gossan evolution and mobility of gold and silver. Ore Geol. Rev. 65, 165–179.

Angelica, R.S., Costa, M.L., Pölmann, H., 1996. Gold, wolframite, tourmaline-bearing lateritized gossans in the Amazon region, Brazil. J. Geochem. Explor. 57, 201–215.

Atapour, H., Aftabi, A., 2007. The geochemistry of gossans associated with Sarcheshmeh porphyry copper deposit, Rafsanjan, Kerman, Iran: implications for exploration and the environment. J. Geochem. Explor. 93, 47–65.

Biagioni, C., Capalbo, C., Pasero, M., 2013. Nomenclature tunings in the hollandite supergroup. Eur. J. Mineral. 25, 85–90.

Biber, M.V., Afonso, M.S., Stumm, W., 1994. The coordination chemistry of weathering: IV. Inhibition of the dissolution of oxide minerals. Geochim. Cosmochim. Acta 58 (9), 1999–2010.

Bigham, J.M., Nordstrom, D.K., 2000. Iron and aluminum hydroxysulfates from acid sulfate waters. In: Alpers, C.N., Jambor, J.L., Nordstrom, D.K. (Eds.), Sulfate Minerals—Crystallography, Geochemistry, and Environmental Significance, Rev. Mineral. Geochem. vol. 40. pp. 351–403.

Bowell, R.J., 1992. Supergene gold mineralogy at Ashanti, Ghana: implications for the supergene behavior of gold. Mineral. Mag. 56, 545–560.

Bowell, R.J., Foster, R.P., Gize, A.P., 1993. The mobility of gold in tropical rain forest soils. Econ. Geol. 88, 999–1016.

Boyle, R.W., 1979. Oxidation and secondary enrichment of gold deposits. In: Boyle, R.W. (Ed.), The Geochemistry of Gold and Its Deposits. vol. 280. Geological Survey of Canada, pp. 431–445.

Costa, M.L., Angelica, R.S., Costa, N.C., 1999. The geochemical association Au–As–B–(Cu)–Sn–W in latosol, colluvium, lateritic iron crust and gossan in Caraja's, Brazil: importance for primary ore identification. J. Geochem. Explor. 67, 33–49.

Cruz, C., Noronha, F., Santos, P., Mortensen, J.K., Lima, A., 2018. Supergene gold enrichment in the Castromil-Serra da Quinta gold deposit, NW Portugal. Mineral. Mag. 82 (S1), 307–320.

Dardenne, M.A., Botelho, N.F., 2014. Metalogênese da Zona Externa da Faixa Brasília. In: Silva, M.G., Rocha Neto, M.T., Jost, H., Kuyunjian, R.M. (Eds.), Metalogênese das Províncias Tetônicas Brasileiras-Programa Geologia do Brasil/Recursos Minerais/Série Metalogenia. CPRM, Belo Horizonte, pp. 431–452.

Dick, J.M., 2008. Calculation of the relative metastabilities of proteins using the CHNOSZ software package. Geochem. Trans. 9 (10).

Dill, H.G., 2015. Supergene alteration of ore deposits: from nature to humans. Elements 11, 311–316.

Dzombak, D.A., Morel, F.M., 1990. Surface Complexation Modeling: Hydrous Ferric Oxide. Wiley, New York (393 pp).

Erlebacher, J., Aziz, M.J., Karma, A., Dimitrov, N., Sieradzki, K., 2001. Evolution of nanoporosity in dealloying. Nature 410, 450–453.

Evans, A.M., 1993. Ore Geology and Industrial Minerals – An Introduction, 3rd edition. Blackwell Scientific Publishing (390pp).

Furley, P.A., 1999. The nature and diversity of neotropical savanna vegetation with particular reference to the Brazilian cerrados. Glob. Ecol. Biogeogr. 8, 223–241.

Gaboreau, S., Vieillard, 2004. Prediction of Gibbs free energies of formation of minerals of the alunite supergroup. Geochim. Cosmochim. Acta 68 (16), 3307–3316.

Goldfarb, R.J., Baker, T., Dubé, B., Groves, D.I., Hart, C.J.R., Gosselin, P., 2005. Distribution, character, and genesis of gold deposits in metamorphic terranes. In: Hedenquist, J.W., Thompson, J.F.H., Goldfarb, R.J., Richards, J.P. (Eds.), Economic Geology 100th Anniversary Volume. Society of Economic Geologists, Littleton, Colorado, USA, pp. 407–450.

Goss, C.J., 1987. The kinetics and reaction mechanism of the goethite to hematite transformation. Mineral. Mag. 51, 437–451.

Gray, D.J., Butt, C.R.M., Lawrance, L.M., 1992. The geochemistry of gold in lateritic terrains. In: Butt, C.R.M., Zeegars, H. (Eds.), Handbook of Exploration Geochemistry 4: Regolith Exploration Geochemistry in Tropical and Subtropical Terrains. Elsevier, Amsterdam, pp. 461–482.

Guilbert, J.M., Park, C.F., 1986. The Geology of Ore Deposits. W.H. Freeman and Co, London (985 pp).

Holmén, B., Casey, W.H., 1996. Hydroxamate ligands, surface chemistry, and the mechanism of ligand-promoted dissolution of goethite [α-FeOOH$_{(s)}$]. Geochim. Cosmochim. Acta 60 (22), 4403–4416.

Kalinin, Y.A., Kovalev, K.R., Naumov, E.A., Kirillov, M.V., 2009. Gold in the weathering crust at the Suzdal' deposit (Kazakhstan). Russ. Geol. Geophys. 50, 174–187.

ICDD, 2018. PDF-4+ 2018 (Database), edited by Dr. Soorya Kabekkodu. International Centre for Diffraction Data, Newtown Square, PA, USA.

Kříbek, B., Zachariáš, J., Knésl, I., Míková, J., Mihaljevič, M., Veselovský, F., Bamba, O., 2016. Geochemistry, mineralogy, and isotope composition of Pb, Zn, and Cu in primary ores, gossan and barren ferruginous crust from the Perkoa base metal deposit, Burkina Faso. J. Geochem. Explor. 168, 49–64.

Laetsch, T., Downs, R., 2006. Software for Identification and Refinement of Cell Parameters From Powder Diffraction Data of Minerals Using the RRUFF Project and American Mineralogist Crystal Structure Databases. Abstracts from the 19th General Meeting of the International Mineralogical Association, Kobe, Japan, 23–28 July 2006.

Larson, L.T., 1970. Cobalt- and nickel-bearing manganese oxides from the Fort Payne Formation, Tennessee. Econ. Geol. 65, 952–962.

Leybourne, M.I., Goodfellow, W.D., Boyle, D.R., Hall, G.E.M., 2000. Form and distribution of gold mobilized into surface waters and sediments from a gossan tailings pile, Murray Brook massive sulphide deposit, New Brunswick, Canada. Appl. Geochem. 15, 629–646.

Mann, A.W., 1984. Mobility of gold and silver in lateritic weathering profiles: some observations from Western Australia. Econ. Geol. 79, 38–49.

Martin, S.T., 2005. Precipitation and dissolution of iron and manganese oxides. In: Grassian, V.H. (Ed.), Environmental Catalysis. CRC Press, Boca Raton, pp. 61–81.

Morrison, G.W., Rose, W.J., Jaireth, S., 1991. Geological and geochemical controls on the silver content (fineness) of gold in gold-silver deposits. Ore Geol. Rev. 6, 333–364.

Nahon, D.B., Herbillon, A.J., Beauvais, A., 1989. The epigenetic replacement of kaolinite by lithiophorite in a manganese–lateritic profile, Brazil. Geoderma 44 (4), 247–259.

Nordstrom, D.K., 2003. Effects of microbiological and geochemical interactions in mine drainage. In: Jambor, J.L., Blowes, D.W., Ritchie, A.I.M. (Eds.), Environmental Aspects of Mine Wastes. vol. 31. Mineralogical Association of Canada, pp. 227–238.

Novello, V.F., 2016. Paleoclima do Centro-Oeste do Brasil desde o último período glacial com base em registro isotópicos de espeleotemas. Unpublished Ph.D. thesis. Universidade de São Paulo, Instituto de Geociências, São Paulo, Brazil (211p).

O'Reilly, S.E., Hochella, M.F., 2003. Lead sorption efficiencies of natural and synthetic Mn and Fe-oxides. Geochim. Cosmochim. Acta 67 (23), 4471–4487.

Paringa Resources, 2012. http://www.paringaresources.com/brazil-gold-graphiteprojects.html, Accessed date: 16 March 2017.

Parkhurst, D.L., Appelo, C.A.J., 2013. Description of input and examples for PHREEQC version 3-a computer program for speciation, batch-reaction, one-dimensional transport, and inverse geochemical calculations. In: U.S. Geological Survey Techniques and Methods, Book 6, (chap. A43, 497 p).

Pires, G.L.C., Bongiolo, E.M., Renac, C., Nascimento, D.B., Prado, M., 2016. Structural and lithological controls of gold-bearing veins associated with the Brasiliano-Pan African Orogeny: an example from the Buracao Area, Arai Group (Brasilia Fold Belt, Brazil). J. S. Am. Earth Sci. 66, 180–195.

Pires, G.L.C., Renac, C., Bongiolo, E.M., Neumann, R., Barats, A., 2019. P–T–X conditions on the genesis of orogenic Au (As, Bi, Ag) deposit in metasedimentary rocks of the Buracão Area, Arai Group, Brasília Fold Belt, Brazil. Ore Geol. Rev. 105, 163–182.

Pracejus, B., Bolton, B.R., Frakes, L.A., 1988. Nature and development of supergene manganese deposits, Groote Eylandt, Northern Territory, Australia. Ore Geol. Rev. 4, 71–98.

Reich, M., Vasconcelos, P.M., 2015. Geological and economical significance of supergene metal deposits. Elements 11, 305–310.

Robb, L.J., 2005. Introduction to Ore-forming Processes. Blackwell Publishing (373 pp).

Scott, K.M., 1987. The mineralogical distribution of pathfinder elements in gossans derived from dolomitic shale-hosted Pb-Zn deposits, Northwest Queensland, Australia. Chem. Geol. 64, 295–306.

Scott, K.M., Ashley, P.M., Lawie, D.C., 2001. The geochemistry, mineralogy and maturity of gossans derived from volcanogenic Zn-Pb-Cu deposits of the eastern Lachlan Fold Belt, NSW, Australia. J. Geochem. Explor. 72, 169–191.

Tanizaki, M.L.N., Campos, J.E.G., Dardenne, M.A., 2015. Estratigrafia do Grupo Arai: registro de rifteamento paleoproteozoico no Brasil Central. Braz. J. Geol. 45 (1), 95–108.

Tardy, Y., Nahon, D., 1985. Geochemistry of laterites, stability of Al-goethite, Al-hematite, and Fe^{3+}-kaolinite in bauxites and ferricretes: an approach to the mechanism of concretion formation. Am. J. Sci. 285, 865–903.

Thornber, M.R., Taylor, G.F., 1992. The mechanisms of sulphide oxidation and gossan formation. In: Butt, C.R.M., Zeegars, H. (Eds.), Handbook of Exploration Geochemistry 4: Regolith Exploration Geochemistry in Tropical and Subtropical Terrains. Elsevier, Amsterdam, pp. 119–138.

Varentsov, I.M., 1996. Manganese Ores of the Supergene Zone: Geochemisty of Formation. Kluwer Academic Publishers, Dordrecht (266 pp).

Vasconcelos, P.M., Kyle, J.R., 1991. Supergene geochemistry and crystal morphology of gold in a semiarid weathering environment: application to gold exploration. J. Geochem. Explor. 40, 115–132.

Vasconcelos, P.M., Reich, M., Shuster, D.L., 2015. The Paleoclimatic Signatures of Supergene Metal Deposits. Elements 11, 317–322.

Velasco, F., Herrero, J.M., Suárez, S., Yusta, I., Alvaro, A., Tornos, F., 2013. Supergene features and evolution of gossans capping massive sulphide deposits in the Iberian Pyrite Belt. Ore Geol. Rev. 53, 181–203.

Vlassopoulos, D., Wood, S., 1990. Gold speciation in natural waters: I. Solubility and hydrolysis reactions of gold in aqueous solution. Geochim. Cosmochim. Acta 54, 3–12.

Vodyanitskii, Y.N., 2009. Mineralogy and geochemistry of manganese: a review of publications. Eurasian Soil Sci. 42 (10), 1170–1178.

Wilson, A.F., 1984. Origin of quartz-free gold nuggets and supergene gold found in laterites and soils – a review and some new observations. J. Geol. Soc. Aust. 31 (3), 303–316.

Wolery, T.J., Sutton, M., 2013. Evaluation of Thermodynamic Data. Lawrence Livermore National Laboratory, USA (LLNL-TR-640133, 38 pp).

Yesares, L., Aiglsperger, T., Sáez, R., Almodóvar, G.R., Nieto, J.M., Proenza, J.A., Gómez, C., Escobar, J.M., 2015. Gold behavior in supergene profiles under changing redox conditions: the example of the Las Cruces Deposit, Iberian Pyrite Belt. Econ. Geol. 110, 2109–2126.

Yesares, L., Sáez, R., Almodóvar, G.R., Nieto, J.M., Gómez, C., Ovejero, G., 2017. Mineralogical evolution of the Las Cruces gossan cap (Iberian Pyrite Belt): from subaerial to underground conditions. Ore Geol. Rev. 80, 377–405.

Zammit, C.M., Shuster, J.P., Gagen, E.J., Southam, G., 2015. The geomicrobiology of supergene metal deposits. Elements 11, 337–342.

Zinder, B., Furrer, G., Stumm, W., 1986. The coordination chemistry of weathering: II. Dissolution of Fe(III) oxides. Geochim. Cosmochim. Acta 50, 1861–1869.